Supporting Information

Noncompetitive Sequential Co-Fe Coordination for High-Density Fe/Co Dual-Atom Catalysts toward Efficient Acidic Oxygen Reduction

Wenjun Li[1], Jiao You[1], Xiaoqing Lin[1], Yan Zhao[1], Yining Zhang*[,2], Zhijun Li[1], Wanglei Wang*[,1], Xiaogang Fu*[,1]

[1]State Key Laboratory of Solidification Processing, Atomic Control & Catalysis Engineering Laboratory (ACCEL), School of Materials Science and Engineering, Northwestern Polytechnical University, Xi'an, Shaanxi, 710072, P. R. China
[2]Yulin Innovation Institute of Clean Energy, Yulin 719000, Shaanxi, China

*Corresponding author email: zhangyn@dnlyl.ac.cn; lwang@nwpu.edu.cn; xiaogangfu@nwpu.edu.cn

Supplementary Figures 1 to 26
Supplementary Tables 1 to 10
Supplementary References

Experimental section

Chemicals

Sulfuric acid (AR, 99%), methanol (AR, 99.5%) and ethanol (AR, 99.5%) were purchased from Sinopharm Chemical Reagent Co., Ltd. (Shanghai, China). 2-Methylimidazole (AR, 98%), cobalt nitrate hexahydrate (AR, 99%) and iron oxide nanoparticles were obtained from Shanghai Macklin Biochemical Technology Co., Ltd. (Shanghai, China). Zinc nitrate hexahydrate, F127 and naphthol (5 wt%) were purchased from Shanghai Aladdin Biochemical Technology Co., Ltd. All reagents in this work could be used without further purification treatment.

Materials characterization

TEM pictures were collected on FEI Talos F200x equipped with a highly sensitive SUPER-X energy dispersive X-ray detector system at 200 kV. The images of single Fe/Co atoms were obtained by a high-angle annular dark-field scanning transmission electron microscopy (HAADF-STEM) on a FEI Themis Z operated at 300 keV, equipped with a probe spherical aberration corrector. The elemental distributions of Fe, N and C were determined by energy-dispersive X-ray spectroscopy (EDS). The crystal phases present in each sample were identified using an Ultima IV with Cu Kα radiation operating at 40 kV and 30 mA. X-ray photoelectron spectroscopy (XPS) measurements were performed on a Thermo ESCALAB 250XI using Al Kα radiation (1486.6 eV) as the X-ray source. Raman spectra were collected using a DXRxi Raman microscope. Inductively coupled plasma mass spectrometry (ICP-MS, Agilent ICP-MS 7900) was applied to determine the concentration of Fe and Co elements in samples. The surface area and micro/mesopore size distributions of the as-prepared materials were determined by the Brunauer-Emmett-Teller (BET) and Density Functional Theory (DFT) methods, respectively. Nitrogen adsorption-desorption isotherm tests were performed on a Micromeritics TriStar II at 77 K. Samples were degassed at 200 °C for 8 h under vacuum prior to nitrogen physisorption measurements.

Electrocatalytic Testing

Electrochemical measurements were carried out by using a Metrohm Autolab (Multi Autolab M204) electrochemical workstation coupled with a rotating-ring disc electrode (RRDE, Pine, AFMSRCE 3005) in a three-electrode cell. A graphite rod and a Hg/HgSO4 (K_2SO_4-sat.) electrode were used as the counter and reference electrodes, respectively. The reference electrode was calibrated to a reversible hydrogen electrode (RHE) in the same electrolyte before each measurement. A rotating disk electrode with a disk diameter of 5 mm (area is 0.19625 cm^2) covered by a thin film of the catalyst was used as the working electrode.

To prepare the working electrode, 10 mg catalysts were ultrasonically dispersed in a 1 mL mixture of 1-propanol and Nafion ionomer (5 wt.%) solution for two hours to get a uniform "ink," and then deposited on a glassy carbon working electrode to reach a catalyst loading of 0.8 mg cm^{-2}. Rotating disk electrode (RDE) polarization plots were recorded in oxygen saturated 0.5 M H_2SO_4 electrolyte by linear stair case voltammetry (SCV) method (potential steps of 30 mV and wait-periods of 30 s) from 1.05 to 0.1 V vs. RHE.

The accelerated durability tests (ASTs) were performed at 30 °C in O_2-saturated 0.5 M H_2SO_4 solution by applying cyclic potential sweeps between 0.6-1.0 V vs. RHE at a sweep rate of 50 mV s^{-1} for 10000 cycles.

Rotating ring-disk electrode (RRDE) measurements were performed using linear sweep voltammetry (LSV) with a potential range of 0.1-1.05 V, a rotation speed of 900 rpm, and a scan rate of 10 mV/s, while the ring electrode potential was held at 1.2 V. The number of electron transfers (n) and hydrogen peroxide yield (% H_2O_2) were calculated by the following equations：

$$H_2O_2\,(\%) = 200 \times \frac{I_R/N}{I_D + I_R/N} \quad (1)$$

$$n = 4 \times \frac{I_D}{I_D + I_R/N} \quad (2)$$

where I_D is the disk current, I_R is the ring current, and N (0.37) is the current collection efficiency of the Pt ring. The electron transfer numbers of ORR were also determined from the slopes of the linear line according to the following K-L equation:

$$\frac{1}{j} = \frac{1}{j_k} + \frac{i}{j_L} = \frac{1}{j_k} + \frac{1}{B\omega^{1/2}} \quad (3)$$

$$B = 0.62nFC_0D_0^{2/3}\nu^{-1/6} \quad (4)$$

where j is the measured current density, j_k is the kinetic current density, j_L is the diffusion-limited current density, ω is the electrode rotation rate, F is Faraday constant (96485 C mol^{-1}), C_0 is the bulk concentration of O_2 (1.2×10^{-3} mol L^{-1}), D_0 is the diffusion coefficient of O_2 (1.9×10^{-5} cm^2 s^{-1}) and ν is the kinetic viscosity of the electrolyte (0.01 cm^2 s^{-1}). ORR results were presented after subtractions of the currents measured in N_2-saturated 0.5 M H_2SO_4 solution to remove capacitive currents.

Quantification of active centers

The SD and TOF were obtained according to the previously reported nitrite reduction method by Kucernak ea al. Briefly, nitrite could interact with Fe metal centre to form stable poisoned

adducts. The poisoned adducts could be stripped entirely in the region of 0.35 to-0.35 V (vs. RHE). The excess coulometric charge Q_{strip} associated with the stripping peak was proportional to the SD:

$$SD(mol\ g^{-1}) = \frac{Q_{strip}(C\ g^{-1})}{n_{strip}F(C\ mol^{-1})} \quad (5)$$

$$TOF(\ s^{-1}) = \frac{n_{strip}\Delta j_k(mA\ cm^{-1})}{Q_{strip}(C\ g^{-1})L_c(mg\ cm^{-2})} \quad (6)$$

where n_{strip} (=5) is the number of transferred electrons per stripped one nitrite. F is Faraday's constant. j_K is the kinetic current density. L_C was the catalyst loading (0.27 mg cm^{-2}). The catalysts were tested without further treatment.

$$Utilization\ of\ sites\ (\%) = \frac{SD(mol\ g^{-1})M(g\ mol^{-1})}{W} \quad (7)$$

where W is the metal contents of C-Fe/Co-N-C or S-Fe/Co-N-C, M is the average atomic mass of Fe and Co for C-Fe/Co-N-C or S-Fe/Co-N-C (based on the ratio of Fe and Co).

ABTs free radical scavenging measurements

ABTs (2,2'-Azinobis-(3-ethylbenzthiazoline-6-sulphonate)) free radical scavenging measurements were conducted according to a method previously reported. For a typical procedure, 4 mg catalysts (S-Fe/Co-N-C, S-Fe-N-C, C-Fe/Co-N-C, and C-Fe-N-C) were added to 5 mL 0.5 M H_2SO_4 solution and then sonicated to form a uniform ink. 2 mM ABTs and 10 mM H_2O_2 were prepared with 0.5 M H_2SO_4 as dilute solution, separately. Firstly, 5 mL 10 mM H_2O_2 and 5 mL 2 mM ABTs solution were mixed. After 10 minutes of reaction, the supernatant was diluted with 0.5 M H_2SO_4 (1:50). Then, 500 μL of catalysts ink were added dropwise to 4 mL of the dilute solution (ABTs+H_2O_2, 1:50). The mixed solution was thoroughly shaken and allowed to react for 7 minutes. Subsequently, the mixed solution was filtered by filter membrane of 0.45 μm. The filtrate was characterized by UV-vis spectra (Lambd 950). The free radical scavenging effect was evaluated by the intensity change in absorbance at 417 nm. Meanwhile the absorbance of the diluted ABTs+H_2O_2 (1:50) solution and the 0.5 M H_2SO_4 solution were also recorded.

In-situ ATR SEIRAS measurement

The test was performed on a Bruker VERTEX 70V platform equipped with a liquid-nitrogen-cooled mercury cadmium telluride detector in O_2 saturated 0.5 M H_2SO_4 electrolyte. The catalyst ink was dropped on a gold film which was chemically deposited on the reflecting plane of a silicon prism. Ag/AgCl electrode was used as the reference electrode. A graphite rod was used as the counter electrode. The electrochemistry data was collected on a CHI760E

workstation. The positive and negative peaks in intensity represent the decrease and increase of the corresponding absorbed intermediates, respectively.

MEAs preparation and PEMFC tests

The catalyst was mixed with Nafion ionomer diluted by isopropanol/water solvent to prepare the catalyst ink. These inks were ultrasonicated for 1 hour and then brushed onto one side of Nafion 211 ionomer membrane with an effective area of ca. 5 cm^2 until the loading reached ca. 4 mg cm^{-2}. Commercial Pt deposited carbon cloth (0.2 mg cm^{-2} Pt, Fuel Cell Etc) as gas diffusion electrode (GDE) was used at the anode. The anode GDE, Nafion membrane with brushed catalysts and gas diffusion layer (GDL, 29 BC, Ion Power) were then assembled by hot-press at 120 °C for five mins using 600 lbs loading to fabricate membrane electrode assemblies (MEA). They were then tested in a single cell and condition-controlled fuel cell test station (Scribner 850e). Both the cell and gas humidifier temperatures were maintained at 80 °C throughout the MEA tests. Back pressures of H_2 and O_2 (air) were both kept at 15 psig, and gas flow rates for H_2 and O_2 (air) were 300 sccm and 500 sccm, respectively.

DFT calculations

All the calculations were performed within the framework of the density functional theory (DFT) as implemented in the Vienna Ab initio Software Package (VASP) code within the Perdew-Burke-Ernzerhof (PBE) generalized gradient approximation and the projected augmented wave (PAW) method. The cutoff energy for the plane-wave basis set was set to 400 eV. Monkhorst–Pack special k-point meshes of 3 × 3 × 1 were proposed to carry out geometry optimization and electronic structure calculation. During the geometry optimization, all atoms were allowed to relax without any constraints until the convergence thresholds of maximum force and energy were smaller than 0.01 eV/Å and 1.0×10^{-5} eV/atom, respectively. A vacuum layer of 15 Å was introduced to avoid interactions between periodic images. The intermolecular van der Waals forces were corrected using the method of DFT-D3.

The Gibbs free energy of each elementary step was calculated as：

$$\Delta G = \Delta E + \Delta ZPE - T\Delta S \quad (8)$$

where ΔE is the total energy difference between the pristine surface and adsorbing surface calculated. ΔZPE and ΔS refer to the change in zero-point energies and entropy during the reaction, respectively. The Gibbs free energy correction for enthalpy and entropy at standard condition (1 atm, 298.15K) was considered.

Supplementary Figures S1-S26

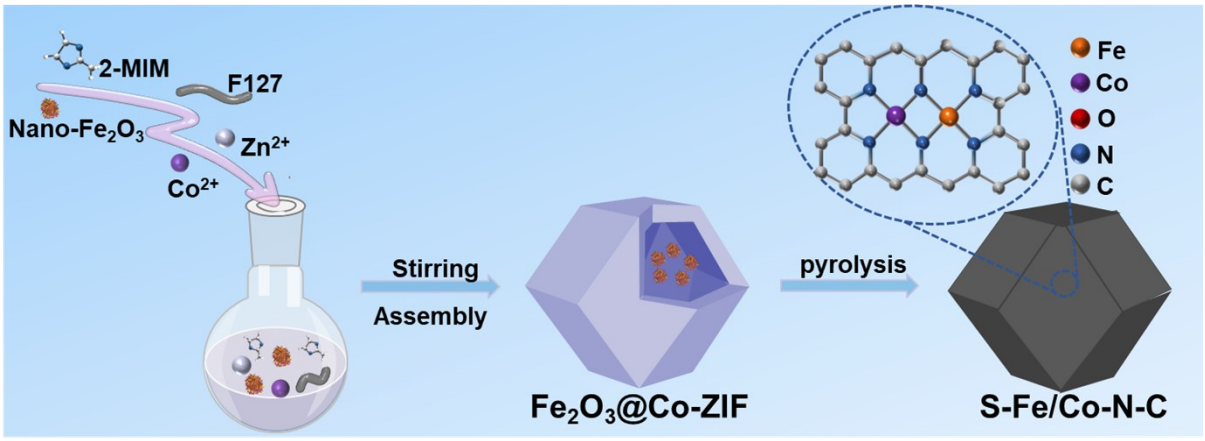

Figure S1. Schematic illustration for the synthesis process of S-Fe/Co-N-C.

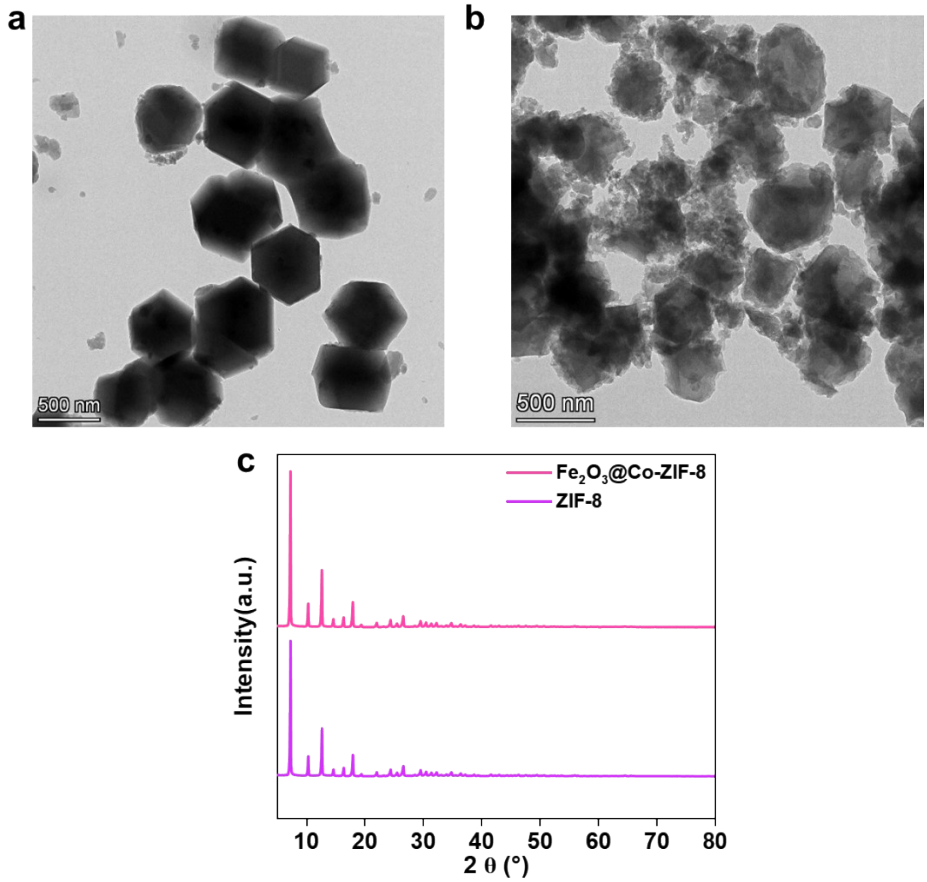

Figure S2. TEM images of (a) Fe_2O_3@Co-ZIF-8 and (b) Fe_2O_3@Co-ZIF-8-Free F127, and (c) XRD patterns of Fe_2O_3@Co-ZIF-8 and ZIF-8.

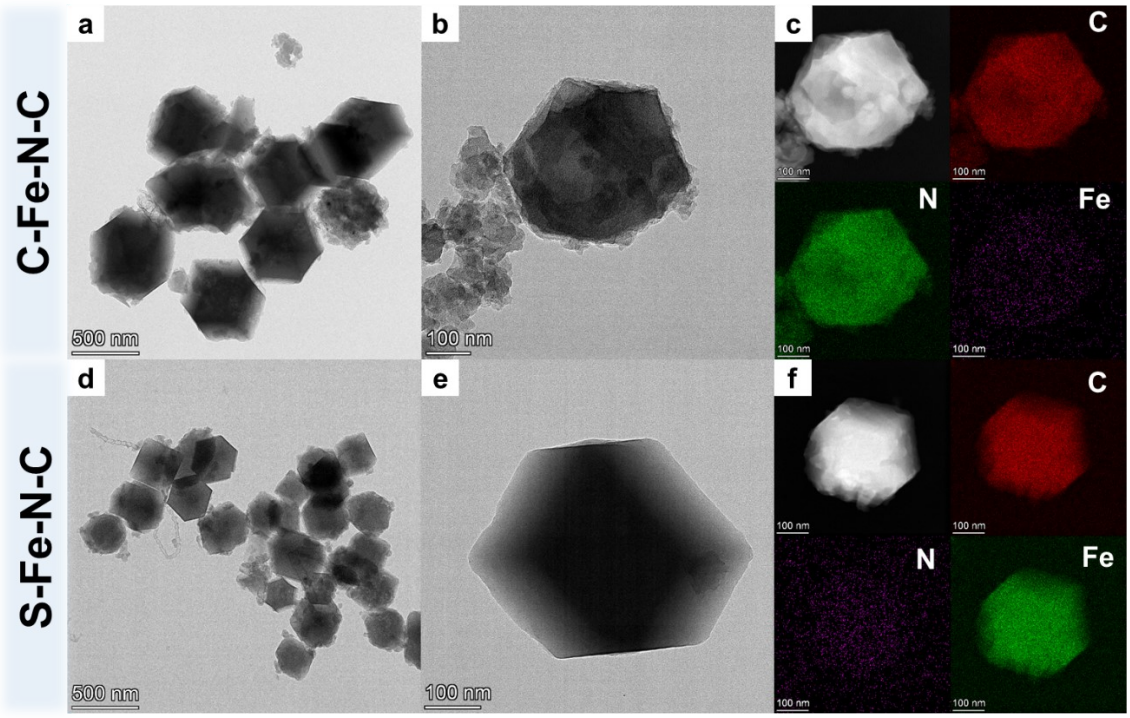

Figure S3. (a, b) TEM images of C-Fe-N-C at different resolutions and (c) corresponding element mappings of C-Fe-N-C; (d, e) TEM images of S-Fe-N-C at different magnifications and (f) corresponding element mappings of S-Fe-N-C.

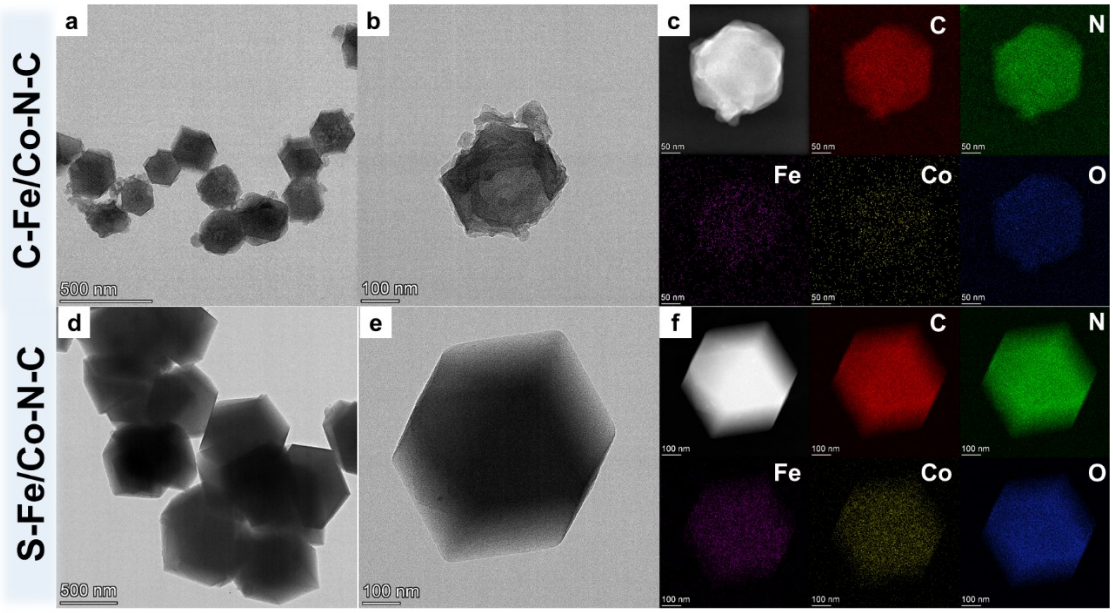

Figure S4. (a, b) TEM images of C-Fe/Co-N-C at different resolutions and (c) corresponding element mappings of C-Fe/Co-N-C; (d, e) TEM images of S-Fe/Co-N-C at different magnifications and (f) corresponding element mappings of S-Fe/Co-N-C.

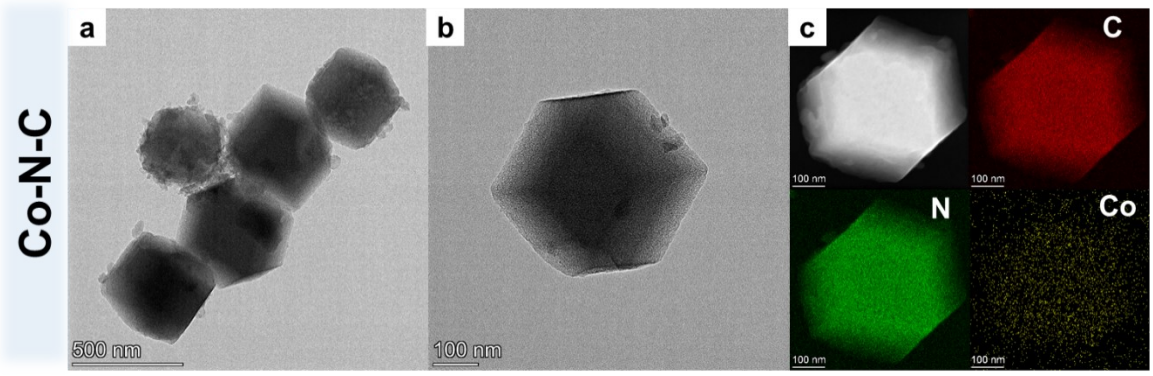

Figure S5. (a, b) TEM images of Co-N-C at different resolutions and (c) corresponding element mappings of Co-N-C.

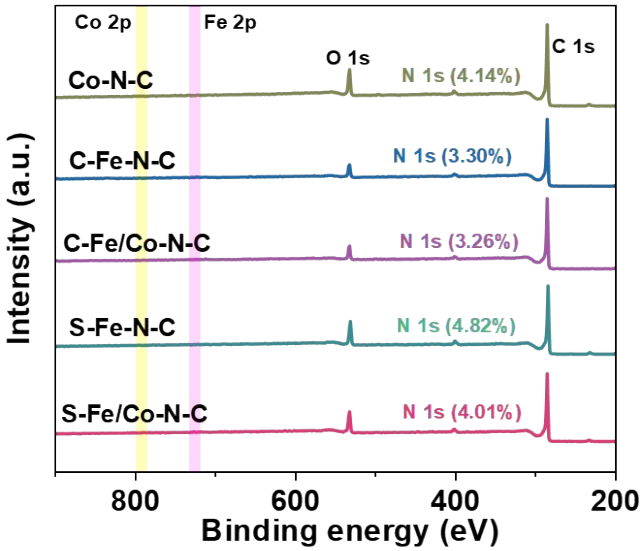

Figure S6. XPS analysis spectra of C-Fe-N-C, C-Fe/Co-N-C, S-Fe-N-C, S-Fe/Co-N-C and Co-N-C.

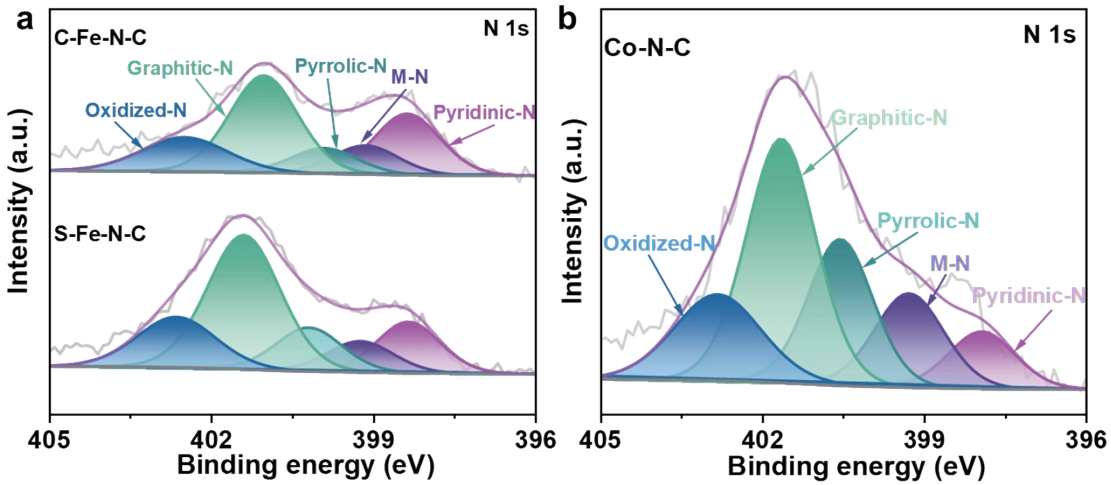

Figure S7. The high-resolution N 1s XPS spectra of (a) C-Fe-N-C and S-Fe-N-C, (b) Co-N-C.

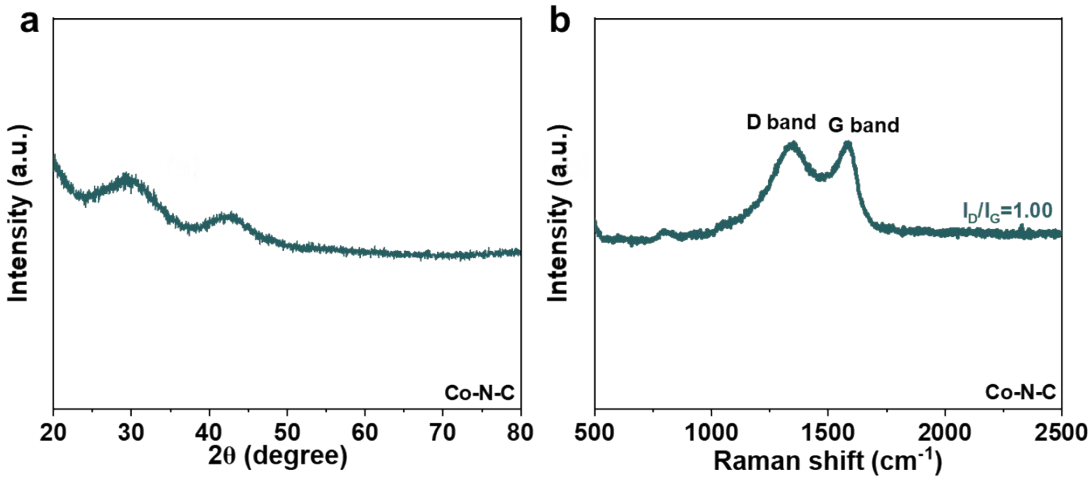

Figure S8. (a) XRD pattern, (b) Raman spectra of Co-N-C.

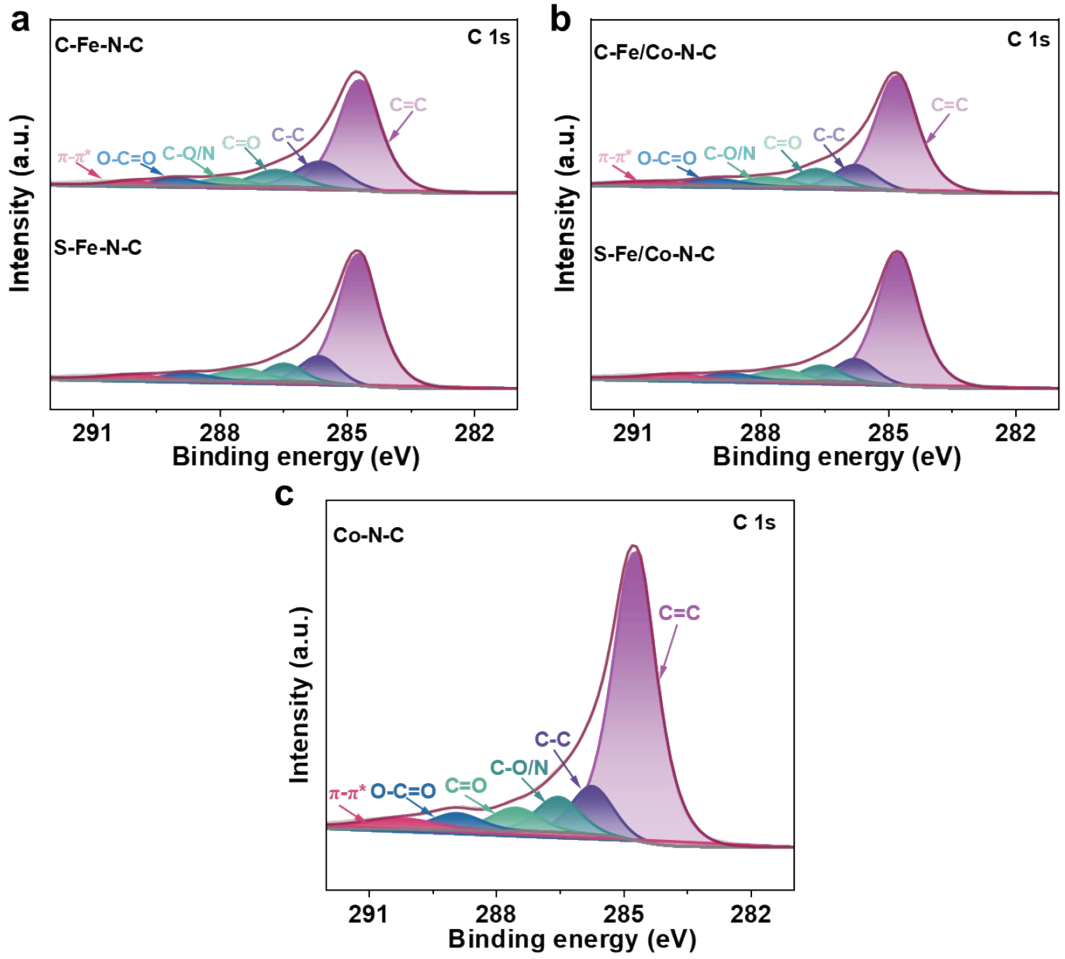

Figure S9. The high-resolution C 1s XPS spectra of (a) C-Fe-N-C and S-Fe-N-C, (b) C-Fe/Co-N-C and S-Fe/Co-N-C, (c) Co-N-C.

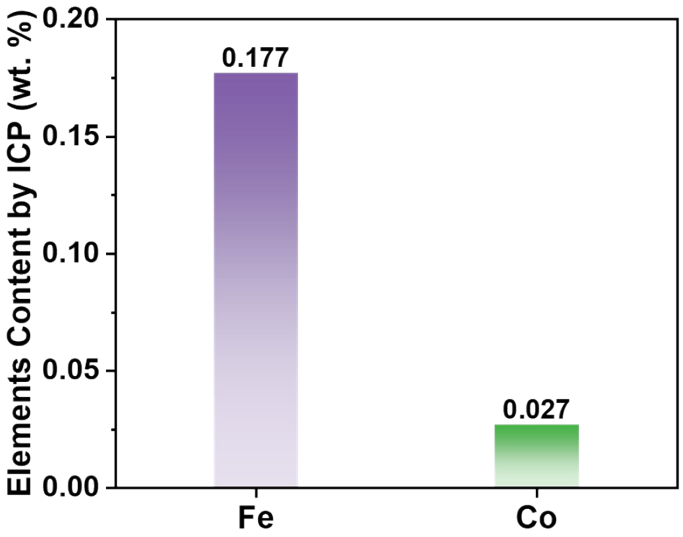

Figure S10. ICP analysis of Fe and Co content in Fe/Co(1:1)-ZIF-8.

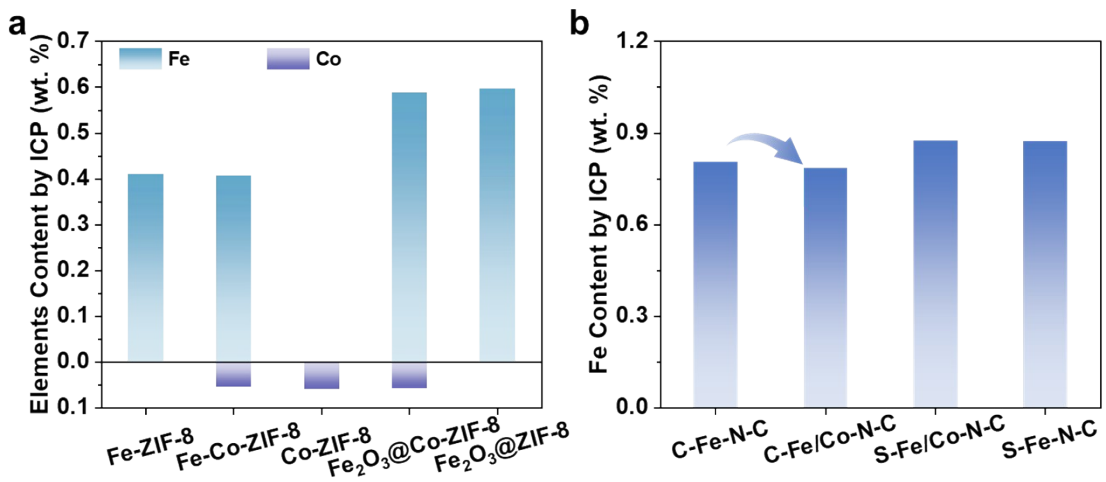

Figure S11. (a) ICP analysis of Fe and Co elements content in Fe-ZIF-8, Fe-Co-ZIF-8, Co-ZIF-8, Fe_2O_3@Co-ZIF-8 and Fe_2O_3@ZIF-8; (b) ICP analysis of Fe content in C-Fe-N-C, C-Fe/Co-N-C, S-Fe/Co-N-C and S-Fe-N-C.

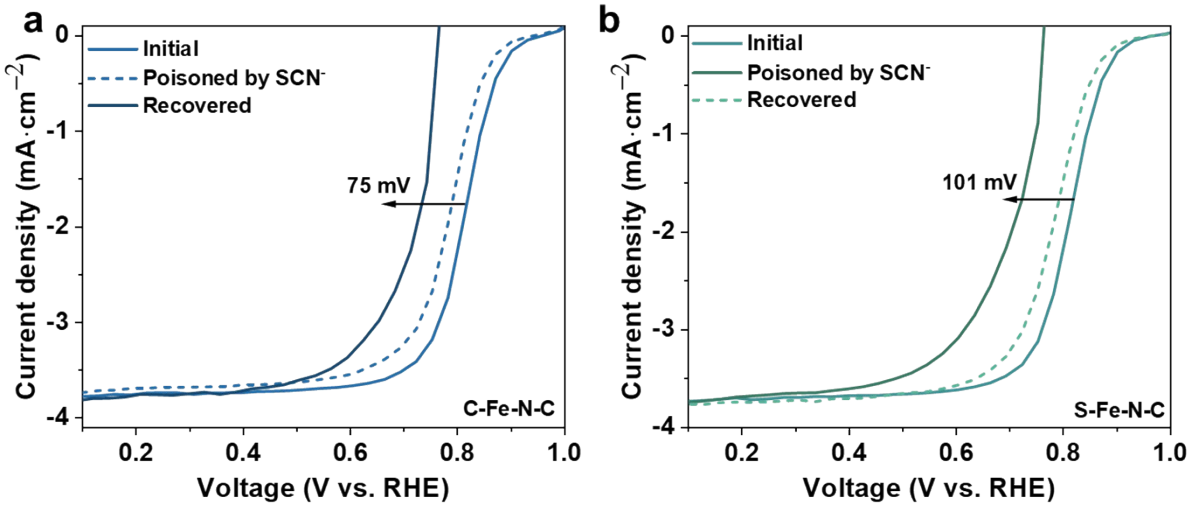

Figure S12. ORR polarization curves of (a) C-Fe-N-C and (b) S-Fe-N-C during SCN^- poisoning and subsequent recovery in 0.5 M H_2SO_4 solution.

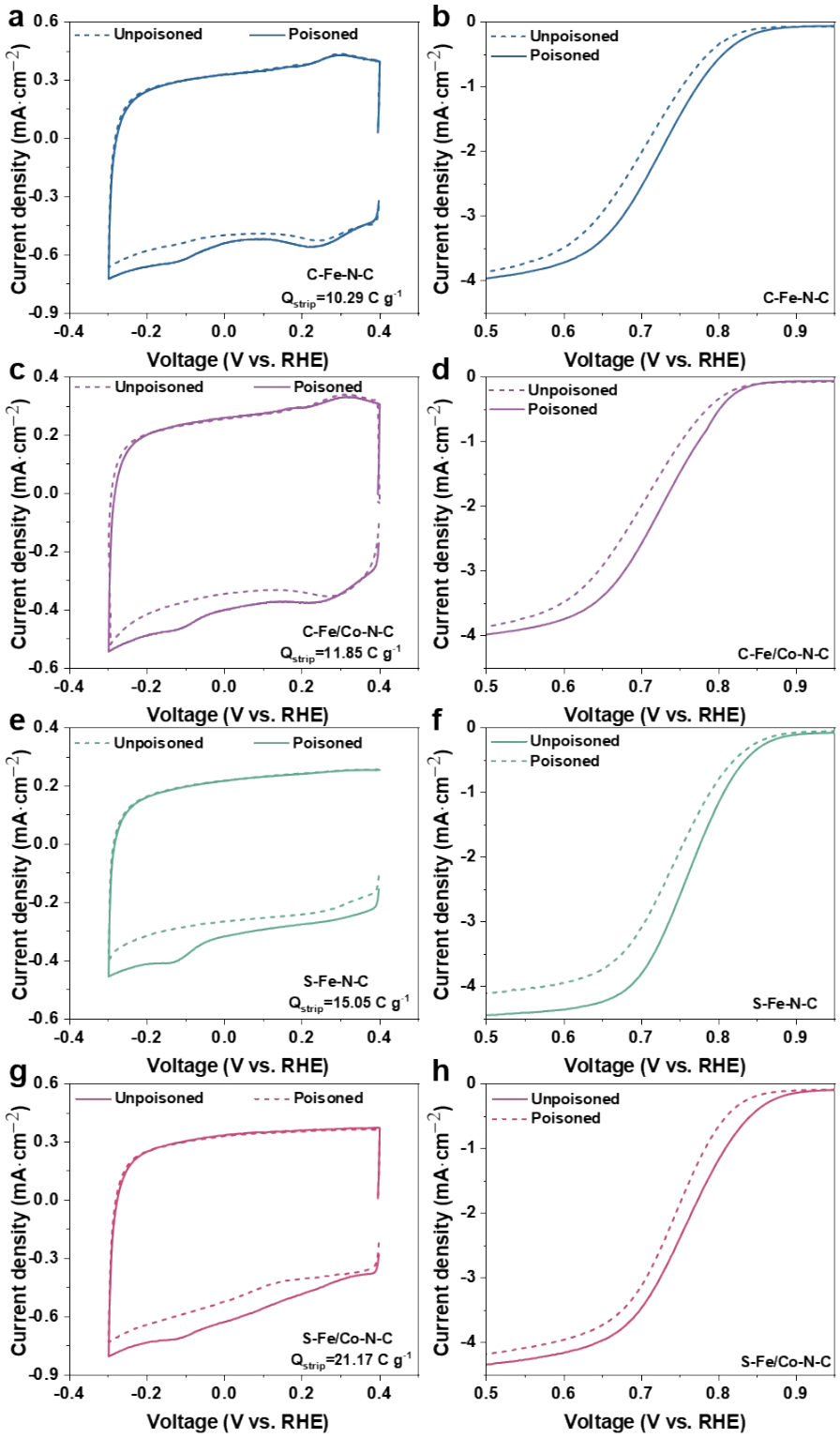

Figure S13. Determination of the SD of (a, b) C-Fe-N-C, (c, d) C-Fe/Co-N-C, (e, f) S-Fe-N-C and (g, h) S-Fe/Co-N-C. (a, c, e, g) CV curves recorded before and during nitrite adsorption in

the nitrite reductive stripping region; (b, d, f, h) LSV curves recorded before and after nitrite adsorption in a 0.5 M acetate buffer at pH 5.2. The catalyst loading was 0.27 mg cm^{-2}.

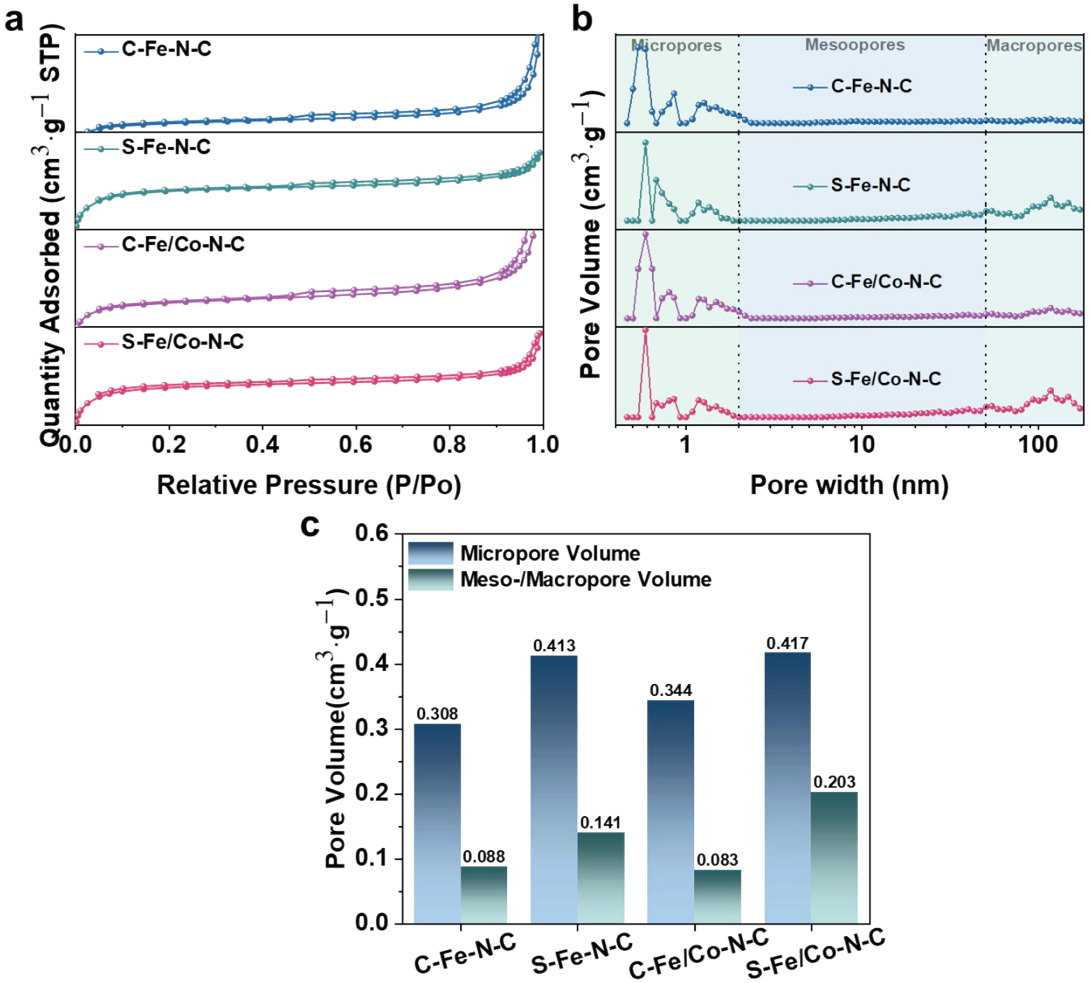

Figure S14. (a) N_2 adsorption-desorption isotherms, (b) pore size distribution curves, and (c) comparison of pore volume of C-Fe-N-C, S-Fe-N-C, C-Fe/Co-N-C, and S-Fe/Co-N-C.

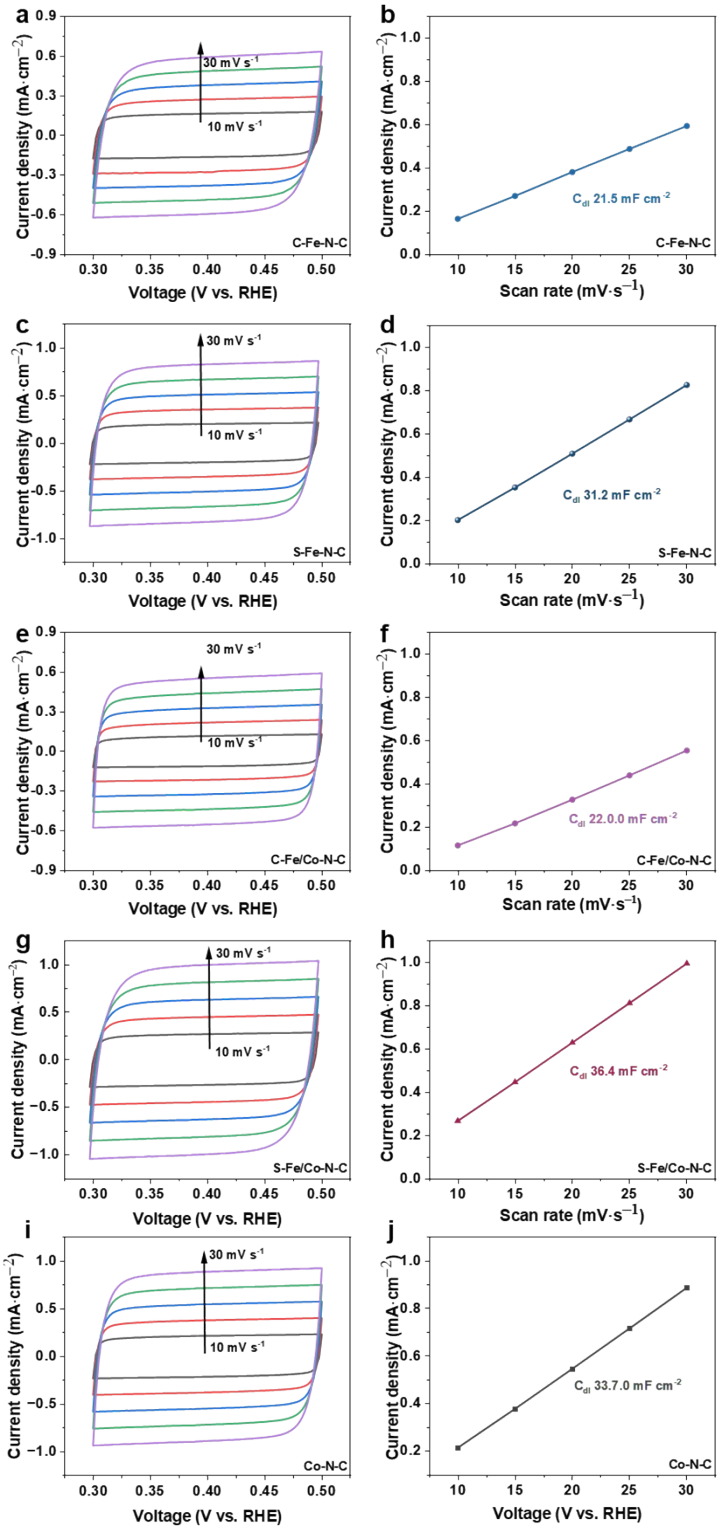

Figure S15. Cyclic voltammograms recorded at various scan rates for (a) C-Fe-N-C, (c) S-Fe-N-C, (e) C-Fe/Co-N-C, (g) S-Fe/Co-N-C, and (i) Co-N-C, with the corresponding linear fits of capacitive current shown in (b), (d), (f), (h), and (j), respectively.

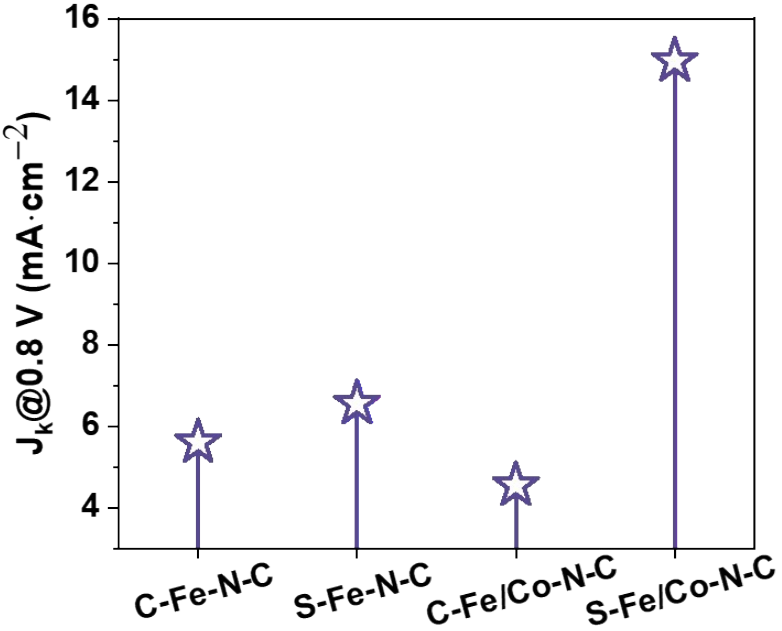

Figure S16. Comparison of J_k at 0.8 V of C-Fe-N-C, S-Fe-N-C, C-Fe/Co-N-C and S-Fe/Co-N-C.

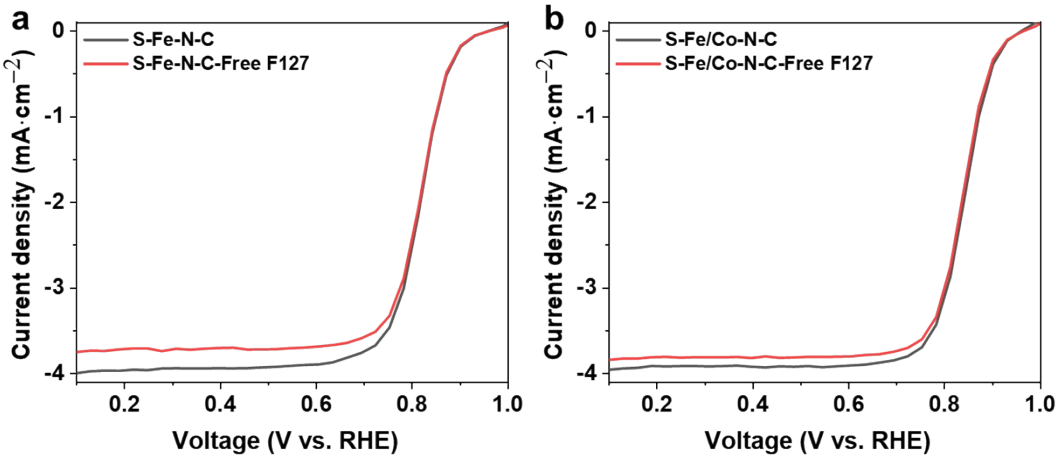

Figure S17. Steady-state ORR polarization plots of (a) S-Fe-N-C and S-Fe-N-C-Free F127, and (b) S-Fe/Co-N-C and S-Fe/Co-N-C-Free F127, measured in O_2-saturated 0.5 M H_2SO_4.

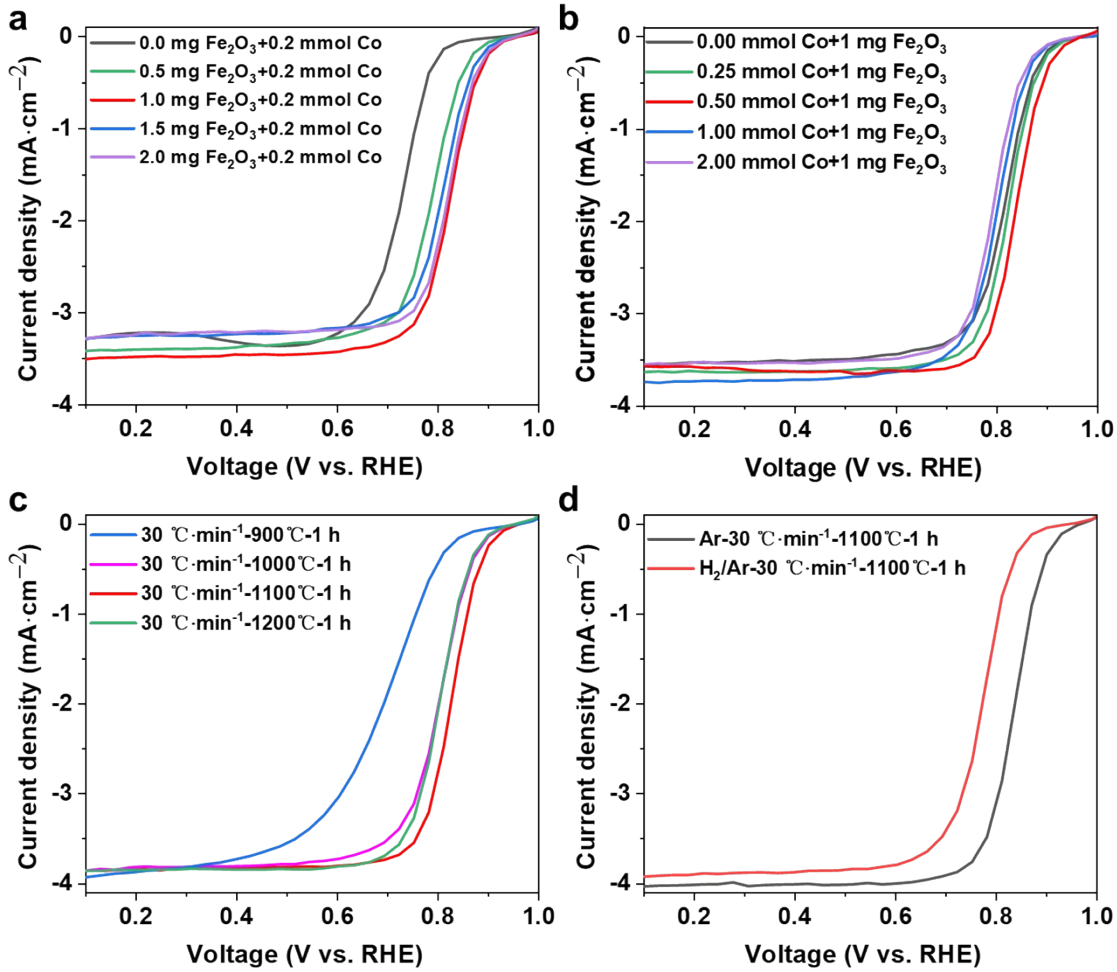

Figure S18. (a, b) Effect of precursor composition regulation on the catalytic performance of S-Fe/Co-N-C; (c, d) Effects of pyrolysis process regulation on the catalytic performance of S-Fe/Co-N-C.

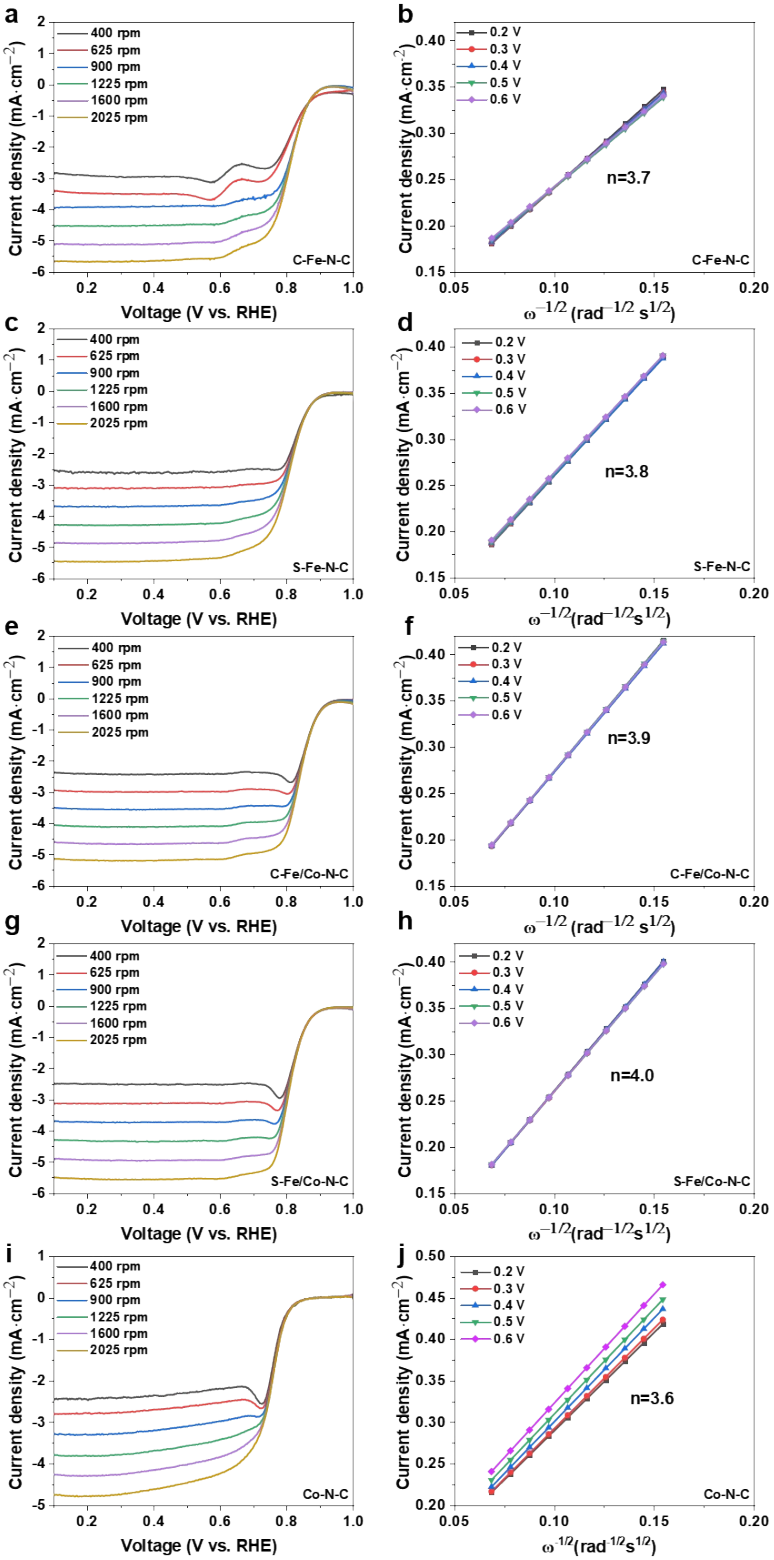

Figure S19. LSV curves at different rotation rates and the corresponding Koutecky-Levich (K-L) plots of (a, b) C-Fe-N-C, (c, d) S-Fe-N-C, (e, f) C-Fe/Co-N-C, (g, h) S-Fe/Co-N-C and (i,j) Co-N-C catalysts in O_2 saturated 0.5 M H_2SO_4 solution.

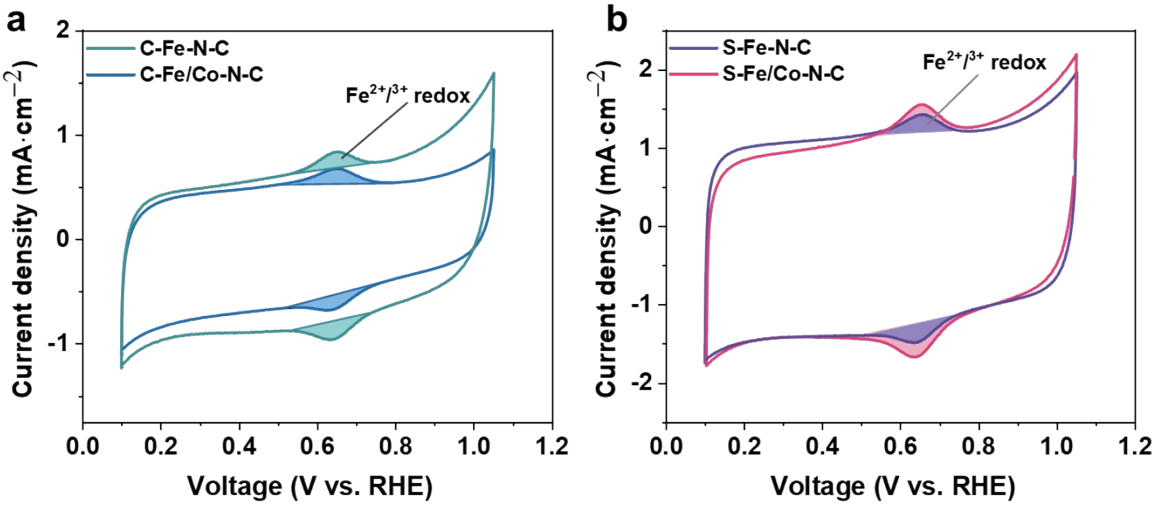

Figure S20. CV curves of (a) C-Fe-N-C, C-Fe/Co-N-C and (b) S-Fe-N-C, S-Fe/Co-N-C collected in Ar-saturated 0.5 M H_2SO_4 electrolyte at room temperature with a scan rate of 10 mV s^{-1}.

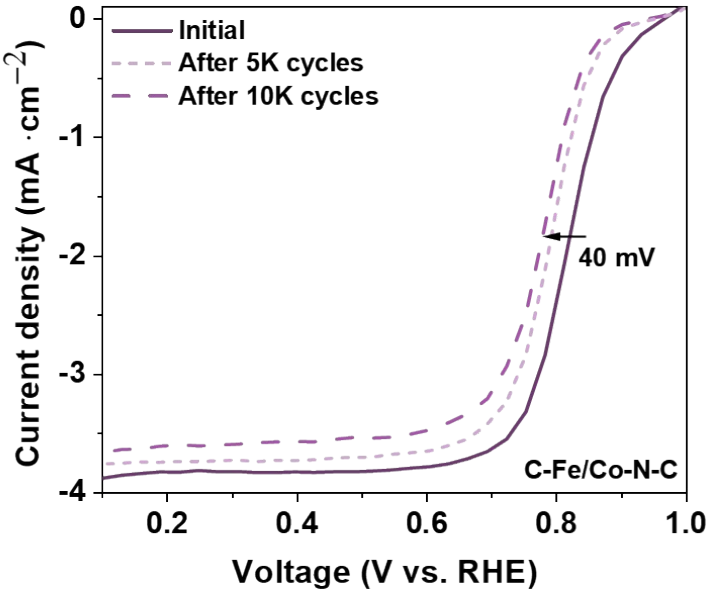

Figure S21. RDE polarization curves of C-Fe/Co-N-C before and after 30, 000 potential cycles ranging from 0.6-1.0 V (vs RHE) in O_2-saturated 0.5 M H_2SO_4.

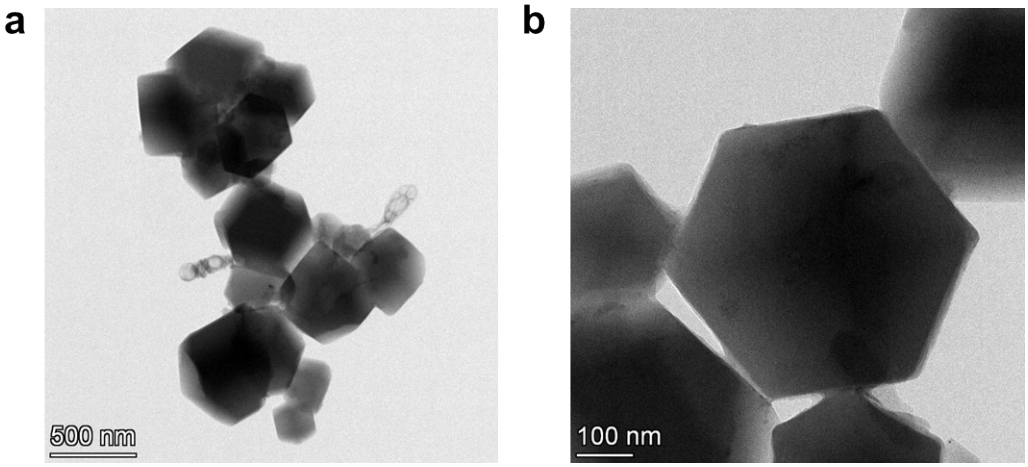

Figure S22. TEM images of S-Fe/Co-N-C-AST.

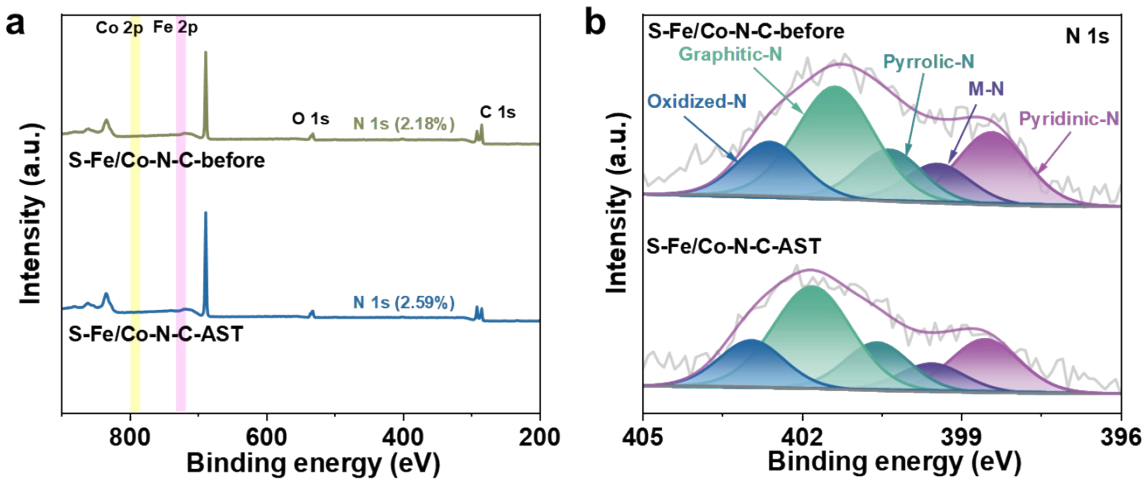

Figure S23. (a) XPS analysis spectra and (b) High-resolution N 1s spectra of S-Fe/Co-N-C and S-Fe/Co-N-C-AST.

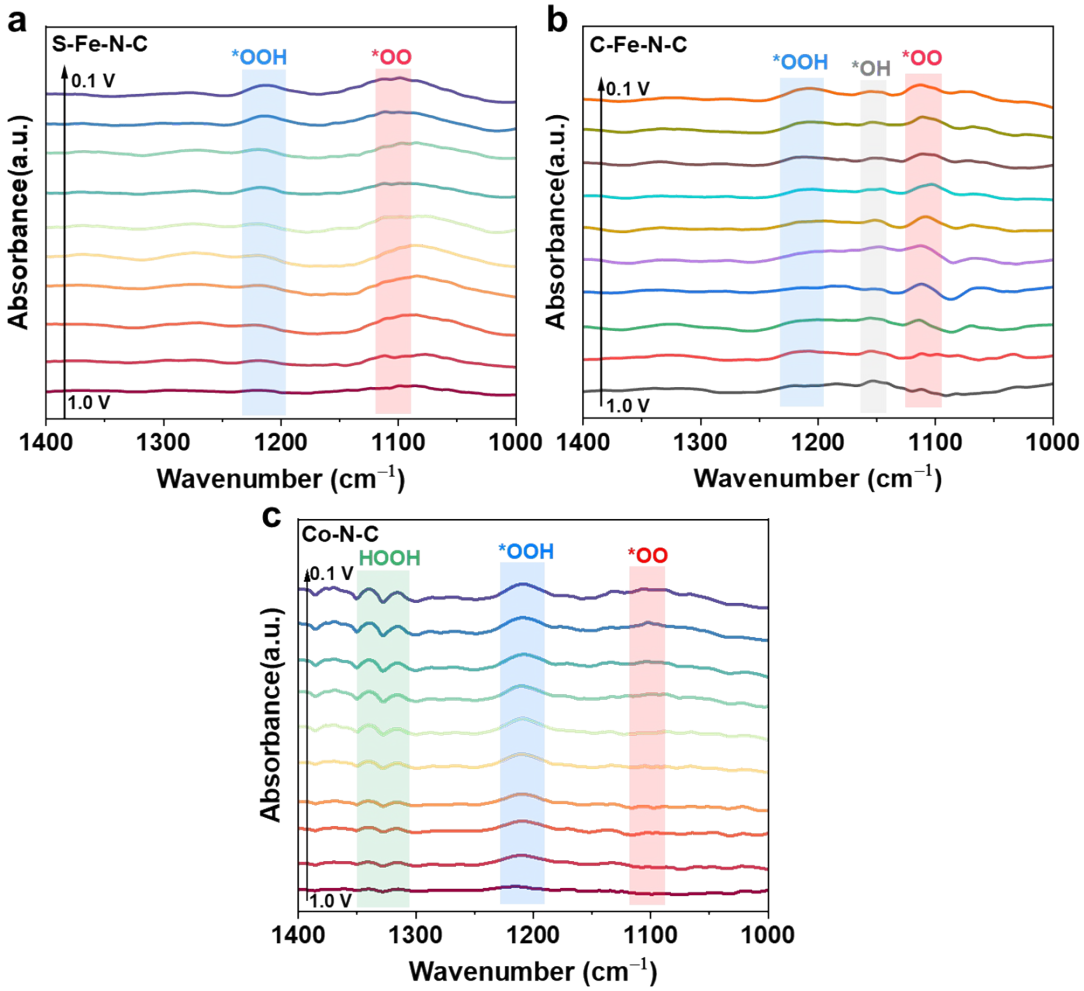

Figure S24. (a) In situ FTIR spectra for (a) S-Fe-N-C, (b) C-Fe-N-C and (c) Co-N-C in 0.5 M H_2SO_4.

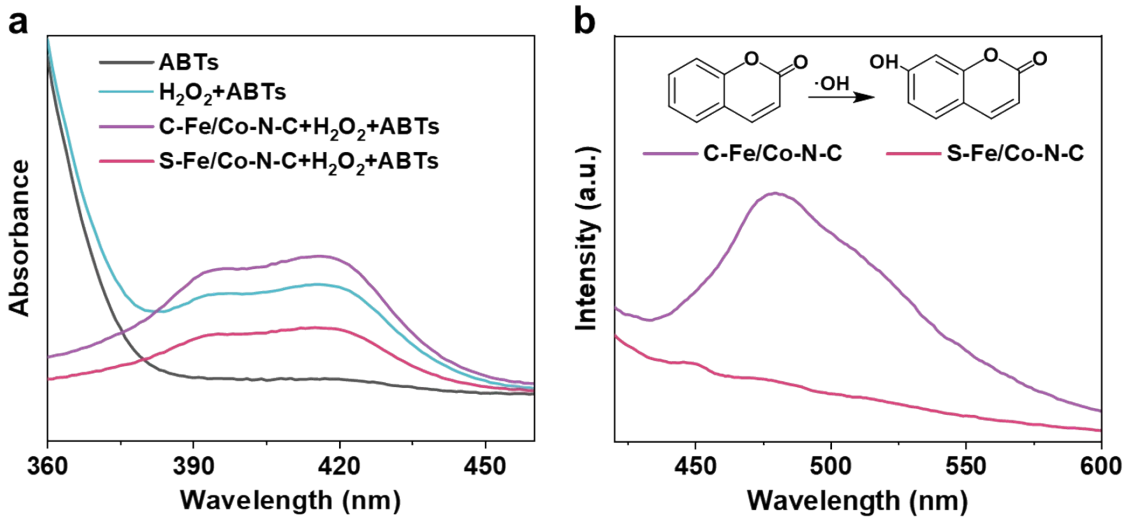

Figure S25. (a) UV-vis absorption spectra of C-Fe/Co-N-C and S-Fe/Co-N-C after 7 min reaction with ABTS + H_2O_2 solution. (b) Fluorescence spectra of C-Fe/Co-N-C and S-Fe/Co-N-C after reaction with coumarin solution for detecting •OH during ORR.

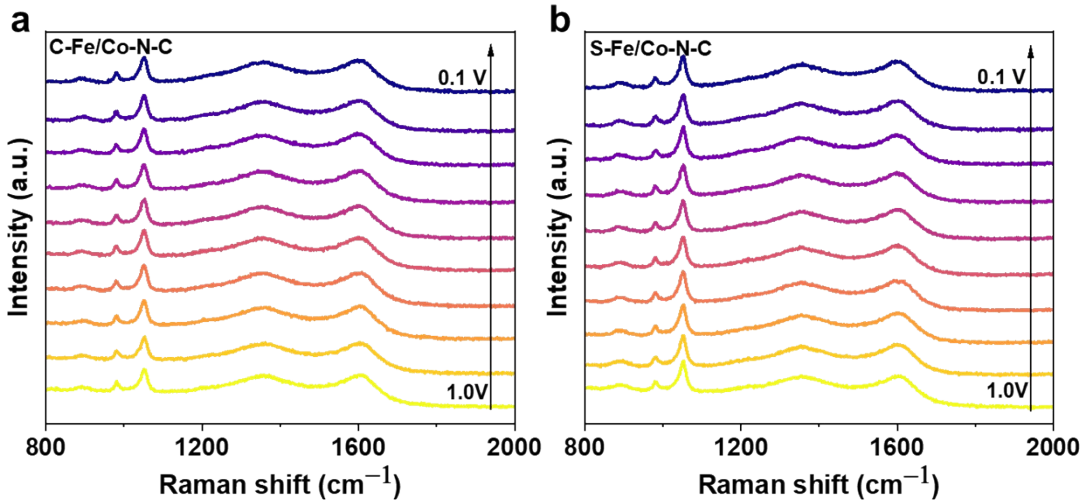

Figure S26. In situ Raman spectra of (a) C-Fe/Co-N-C and (b) S-Fe/Co-N-C catalysts recorded during the ORR process.

Table S1. Elemental compositions of the as-prepared C-Fe-N-C, S-Fe-N-C, C-Fe/Co-N-C, S-Fe/Co-N-C and Co-N-C catalysts determined by XPS (at%).

simple	C(at%)	N(at%)	O(at%)	Co(at%)	Fe(at%)	Zn(at%)
C-Fe-N-C	87.73	3.30	8.72	-	0.13	0.12
S-Fe-N-C	81.44	4.82	13.35	-	0.14	0.24
C-Fe/Co-N-C	88.24	3.26	7.97	0.17	0.13	0.23
S-Fe/Co-N-C	82.56	4.01	13.03	0.16	0.05	0.19
Co-N-C	82.68	12.93	4.14	0.17	-	0.07

Table S2. XPS data of surface N species for the different catalysts.

Sample	Pyridinic-N (%)	M-N (%)	Pyrrolic-N (%)	Graphitic-N (%)	Oxide-N (%)
C-Fe-N-C	23.55 （398.38）	11.11 (399.15)	9.84 (399.92)	38.57 (401.03)	16.92 (402.50)
S-Fe-N-C	14.83 （398.36）	9.41 (399.25)	13.19 (400.20)	44.54 (401.40)	18.03 (402.65)
C-Fe/Co-N-C	21.89 （398.48）	9.90 (399.18)	11.63 (399.90)	35.86 (401.03)	20.70 (402.49)
S-Fe/Co-N-C	16.38 （398.52）	7.53 (399.36)	13.15 (400.11)	46.69 (401.44)	16.26 (402.71)
Co-N-C	5.60 （397.91）	17.82 (399.50)	19.28 (400.68)	42.89 (401.65)	14.41 (402.70)

Table S3. XPS data of surface C species for the different catalysts.

Sample	C=C (%)	C-C (%)	C-O/N (%)	C=O (%)	O-C=O (%)	Π-Π* (%)
C-Fe-N-C	54.54 (284.70)	21.66 (285.42)	14.15 (286.43)	3.26 (287.77)	4.02 (288.66)	2.37 (290.08)
S-Fe-N-C	64.65 (284.70)	10.67 (285.66)	7.21 (286.49)	6.30 (287.47)	3.50 (288.79)	7.67 (290.00)
C-Fe/Co-N-C	49.12 (284.66)	16.11 (284.43)	11.18 (286.17)	14.18 (287.05)	7.01 (289.03)	2.40 (290.59)
S-Fe/Co-N-C	66.69 (284.73)	9.72 (285.79)	6.62 (286.57)	5.38 (287.54)	3.29 (288.75)	8.31 (289.98)
Co-N-C	56.09 (284.69)	18.12 (285.43)	12.81 (286.34)	5.92 (287.67)	6.62 (289.25)	0.44 (290.19)

Table S4. ICP-MS analysis of different samples.

Catalysts	Fe content(wt%)	Co content(wt%)
Co-ZIF-8	---	0.058
Fe_2O_3@ZIF-8	0.597	---
Fe_2O_3@Co-ZIF-8	0.580	0.056
Fe-ZIF-8	0.411	---
Fe-Co-ZIF-8	0.407	0.054
Fe/Co(1:1)-ZIF-8	0.177	0.027

Table S5. ICP-MS analysis of different samples.

Catalysts	Fe content(wt%)	Co content(wt%)
Co-N-C	---	0.145
S-Fe-N-C	0.873	---
S-Fe/Co-N-C	0.876	0.139
C-Fe-N-C	0.806	---
C-Fe/Co-N-C	0.785	0.047

Table S6. Summary of the SD, TOF, and iron utilization of different catalysts determined by the nitrite stripping experiment.

Catalysts	Q_{strip} (C g^{-1})	SD (μmol g^{-1})	SD (sites g^{-1})	ΔJ_k@0.82 (mA cm^{-2})	TOF@0.82 (s^{-1})
C-Fe-N-C	10.29	21.26	1.28×10^{19}	0.207	0.373
C-Fe/Co-N-C	11.85	24.44	1.47×10^{19}	0.235	0.367
S-Fe-N-C	15.05	31.19	1.88×10^{19}	0.377	0.463
S-Fe/Co-N-C	21.17	43.85	2.64×10^{19}	0.594	0.520

Table S7. Summary of the SD and utilization of sites of different catalysts determined by the nitrite stripping experiment.

Catalysts	SD ($\mu mol\ g^{-1}$)	Fe content (wt. %)	Co content (wt. %)	Utilization of sites (%)
C-Fe-N-C	21.26	0.806	---	14.73
C-Fe/Co-N-C	24.44	0.785	0.047	16.65
S-Fe-N-C	31.19	0.873	---	19.95
S-Fe/Co-N-C	43.85	0.876	0.139	24.30

Table S8. Comparison of BET surface areas and volume in various materials.

Simples	S_{BET} ($m^2\ g^{-1}$)	V_{micro} ($cm^3\ g^{-1}$)	$V_{meso/macro}$ ($cm^3\ g^{-1}$)	SD_{BET} (sites m^{-2})
C-Fe-N-C	866.6	0.308	0.088	1.48×10^{16}
C-Fe/Co-N-C	971.2	0.344	0.083	1.51×10^{16}
S-Fe-N-C	1085.3	0.413	0.141	1.73×10^{16}
S-Fe/Co-N-C	1076.9	0.417	0.203	2.45×10^{16}

Table S9. Comparison of the ORR activity of S-Fe/Co-N-C catalyst with reported non-precious metal catalysts in acidic electrolyte.

Electrocatalysts	**$E_{1/2}$**	**E_{onset}**	**Ref.**
S-Fe/Co-N-C	0.842	0.94	This work
$FeCoN_x/C$	0.86	1.02	J. Am. Chem. Soc. 2019[1]
Spa-S-Fe,Co/NC	0.846	0.98	Sci.Adv. 2023[2]
FeCo-N-HCN	0.75	0.91	Adv. Funct. Mater. 2021[3]
CoFe-NC	0.804	0.938	J. Mater. Chem. A,2021[4]
Fe,Mn/N-C	0.804	0.97	Nat Commun. 2021[5]
Fe(Zn)-N-C	0.83	0.93	Angew.Chem. 2020[6]
Fe-Mn-N-C	0.79	1.0	Appl. Catal. B: Environ. 2022[7]
FeCo-NC-3	0.842	0.982	J. Mater. Chem. A, 2022[8]
M/FeCo-SAs-N-C	0.851	0.981	Angew.Chem. 2020[9]
Co_2/Fe-N@CHC	0.812	0.96	Adv. Mater. 2021[10]
Zn/CoN-C	0.796	0.97	Angew.Chem.2019[11]
Co_4/Fe_1@NC	0.835	0.98	Angew.Chem. 2023[12]
Fe_2–$S_1N_5N_5$/SNC	0.829	0.929	Energy Environ. Sci.[13]
(FeMn-DA)-N-^{4}C	0.82	0.94	Nano-Micro Lett. 2025[14]
Fe@Fe-N-C	0.829	0.952	Small 2023 [15]
ZnCo-NC-II	0.786	0.941	Appl. Catal. B: Environ. 2022[16]

Table S10. ICP-MS analysis of Fe and Co dissolution amounts for S-Fe/Co-N-C and C-Fe/Co-N-C.

Catalysts	Fe content ($\mu g \cdot L^{-1}$)	Co content ($\mu g \cdot L^{-1}$)
S-Fe/Co-N-C	65.31	36.55
C-Fe/Co-N-C	144.59	89.59

References

1 M. Xiao, Y. Chen, J. Zhu, H. Zhang, X. Zhao, L. Gao, X. Wang, J. Zhao, J. Ge, Z. Jiang, S. Chen, C. Liu and W. Xing, *J. Am. Chem. Soc.*, 2019, **141**, 17763-17770.

2 F. Liu, L. Shi, X. Lin, B. Zhang, Y. Long, F. Ye, R. Yan, R. Cheng, C. Hu, D. Liu, J. Qiu and L. Dai, *Sci. Adv.*, 2023, **9**, eadg0366.

3 H. Li, Y. Wen, M. Jiang, Y. Yao, H. Zhou, Z. Huang, J. Li, S. Jiao, Y. Kuang and S. Luo, *Adv. Funct. Mater.*, 2021, **31**, 2011289.

4 K. Wang, *J. Mater. Chem. A.*, 2021, **9**, 13044-13055.

5 G. Yang, J. Zhu, P. Yuan, Y. Hu, G. Qu, B.-A. Lu, X. Xue, H. Yin, W. Cheng, J. Cheng, W. Xu, J. Li, J. Hu, S. Mu and J.-N. Zhang, *Nat. Commun.*, 2021, **12**, 1734.

6 L. Gong, H. Zhang, Y. Wang, E. Luo, K. Li, L. Gao, Y. Wang, Z. Wu, Z. Jin, J. Ge, Z. Jiang, C. Liu and W. Xing, *Angew. Chem. Int. Ed.*, 2020, **132**, 14027-14032.

7 S. Huang, Z. Qiao, P. Sun, K. Qiao, K. Pei, L. Yang, H. Xu, S. Wang, Y. Huang, Y. Yan and D. Cao, *Appl. Catal. B.*, 2022, **317**, 121770.

8 Y. Chen, J. Li, Y. Zhu, J. Zou, H. Zhao, C. Chen, Q. Cheng, B. Yang, L. Zou, Z. Zou and H. Yang, *J. Mater. Chem. A.*, 2022, **10**, 9886-9891.

9 S. Yin, J. Yang, Y. Han, G. Li, L. Wan, Y. Chen, C. Chen, X. Qu, Y. Jiang and S. Sun, *Angew. Chem. Int. Ed.*, 2020, **132**, 22160–22163.

10 Z. Wang, X. Jin, C. Zhu, Y. Liu, H. Tan, R. Ku, Y. Zhang, L. Zhou, Z. Liu, S. Hwang and H. J. Fan, *Adv. Mater.*, 2021, **33**, 2104718.

11 Z. Lu, B. Wang, Y. Hu, W. Liu, Y. Zhao, R. Yang, Z. Li, J. Luo, B. Chi, Z. Jiang, M. Li, S. Mu, S. Liao, J. Zhang and X. Sun, *Angew. Chem. Int. Ed.*, 2019, **131**, 2648-2652.

12 Y. Zhou, W. Yang, W. Utetiwabo, Y. Lian, X. Yin, L. Zhou, P. Yu, R. Chen and S. Sun, *J. Phys. Chem. Lett.*, 2020, **11**, 1404-1410.

13 Y. Li, X. Luo, Z. Wei, F. Zhang, Z. Sun, Z. Deng, Z. Zhan, C. Zhao, Q. Sun, L. Zhang, W. Chen, S. Li and S. Pang, *Energy Environ. Sci.*, 2024, **17**, 4646-4657.

14 L. Zhang, Y. Dong, L. Li, Y. Shi, Y. Zhang, L. Wei, C.-L. Dong, Z. Lin and J. Su, *Nano-Micro Lett.*, 2025, **17**, 88.

15 L. Li, Y. Wen, G. Han, F. Kong, L. Du, Y. Ma, P. Zuo, C. Du and G. Yin, *Small.*, 2023, **19**, 2300758.

16 K. Song, Y. Feng, X. Zhou, T. Qin, X. Zou, Y. Qi, Z. Chen, J. Rao, Z. Wang, N. Yue, X. Ge, W. Zhang and W. Zheng, *Appl. Catal. B.*, 2022, **316**, 121591.